HHS Public Access

Author manuscript

Mol Imaging Biol. Author manuscript; available in PMC 2019 April 01.

Published in final edited form as:

Mol Imaging Biol. 2018 April ; 20(2): 230–239. doi:10.1007/s11307-017-1122-6.

In vivo Biodistribution of Radiolabeled Acoustic Protein Nanostructures

Johann Le Floc'h[iD,1], **Aimen Zlitni**[2], **Holly A. Bilton**[2], **Melissa Yin**[1], **Arash Farhadi**[3], **Nancy R. Janzen**[2], **Mikhail G. Shapiro**[3], **John F. Valliant**[2], and **F. Stuart Foster**[1]

[1]Sunnybrook Research Institute, 2075 Bayview Avenue, Room S640, Toronto, ON, M4N 3M5, Canada

[2]Department of Chemistry and Chemical Biology, McMaster University, 1280 Main Street West, Hamilton, ON, L8S4L8, Canada

[3]Division of Chemistry and Chemical Engineering, California Institute of Technology, Pasadena, CA, USA

Abstract

Purpose—Contrast-enhanced ultrasound plays an expanding role in oncology, but its applicability to molecular imaging is hindered by a lack of nanoscale contrast agents that can reach targets outside the vasculature. Gas vesicles (GVs)—*a unique class of gas-filled protein nanostructures*—have recently been introduced as a promising new class of ultrasound contrast agents that can potentially access the extravascular space and be modified for molecular targeting. The purpose of the present study is to determine the quantitative biodistribution of GVs, which is critical for their development as imaging agents.

Procedures—We use a novel bioorthogonal radiolabeling strategy to prepare technetium-99m-radiolabeled ([^{99m}Tc])GVs in high radiochemical purity. We use single photon emission computed tomography (SPECT) and tissue counting to quantitatively assess GV biodistribution in mice.

Results—Twenty minutes following administration to mice, the SPECT biodistribution shows that 84 % of [^{99m}Tc]GVs are taken up by the reticuloendothelial system (RES) and 13 % are found in the gall bladder and duodenum. Quantitative tissue counting shows that the uptake (mean ± SEM % of injected dose/organ) is 0.6 ± 0.2 for the gall bladder, 46.2 ± 3.1 for the liver, 1.91 ± 0.16 for the lungs, and 1.3 ± 0.3 for the spleen. Fluorescence imaging confirmed the presence of GVs in RES.

Correspondence to: Johann Le Floc'h; jlefloch@sri.utoronto.ca, John Valliant; valliant@mcmaster.ca.
Johann Le Floc'h and Aimen Zlitni contributed equally to this work.
Johann Le Floc'h http://orcid.org/0000-0003-0010-5120

Electronic supplementary material The online version of this article (https://doi.org/10.1007/s11307-017-1122-6) contains supplementary material, which is available to authorized users.

Compliance with Ethical Standards. All experimental procedures were approved by the Animal Care Committees at Sunnybrook Research Institute and McMaster University.

Conflict of Interest
The authors declare that they have no conflict of interest.

Conclusions—These results provide essential information for the development of GVs as targeted nanoscale imaging agents for ultrasound.

Keywords

Ultrasound contrast agent; Acoustic nanostructures; Gas vesicles; Biodistribution; SPECT/CT; Bioorthogonal chemistry; Technetium-99m

Introduction

Contrast-enhanced ultrasound (CEUS), with lipid- or protein-stabilized gas microbubbles, plays an important role in patient care and is evolving as a fundamental screening tool in cardiology, oncology and gynecology [1]. CEUS is used in a variety of clinical applications such as detecting and characterizing focal liver lesions [2], evaluating cerebral circulation for stroke [3], brain death diagnosis [4], kidney [5], liver and pancreas cancer prognosis, and contrast echocardiography [6–9]. The majority of these clinical applications are based on perfusion imaging and utilize conventional untargeted microbubbles.

Considerable efforts have been directed toward the development of targeted microbubbles to allow visualization of specific biomarkers of disease using CEUS (*i.e.*, molecular imaging). Unfortunately, after two decades of investigation, there is only one example of molecular ultrasound imaging in the clinic, *i.e.*, targeted ultrasound imaging of kinase insert domain receptor in prostate [10, 11], ovarian, and breast cancer patients [12]. The limited number of agents undergoing advanced testing is due to both regulatory issues and limitations of existing microbubbles, which are restricted to the vascular space due to their large size and limited *in vivo* stability (seconds to minutes). Furthermore, other candidates including solid [13], liquid [14], hollow, or phase-change contrast agents have been investigated and demonstrate weak echogenicity [15, 16] and poor stability and require cumbersome synthesis. As a result and to maximize the utility of targeted molecular ultrasound imaging, there is a need to discover and fully characterize novel nanosized ultrasound imaging agents with strong echogenicity, longer *in vivo* stability, and modifiable surface to allow the agents to bind to a wider array of disease biomarkers.

A promising ultrasound contrast model based on naturally occurring nanostructures, called gas vesicles (GVs), has been reported [17]. The biological function of the GVs is to provide buoyancy to a wide range of aqueous haloarchaea and cyanobacteria. GVs have been studied for over 100 years [18], resulting in considerable knowledge of their biochemical and genetic structure [19]. GVs are gas-filled, protein-shelled nanostructures with typical widths of 45–250 nm and lengths of 100–600 nm that exclude water and are permeable to gas [20]. Because of these properties, Shapiro *et al.* recently explored the potential of GVs for contrast enhanced ultrasound imaging [17]. They showed that GVs exhibit non-linear ultrasonic properties, which could be due to buckling [21], substantially improve contrast in ultrasound images and have no adverse side effects in mice. Due to their small volume, they have the potential to access extravascular targets *via* the enhanced and permeable retention effect [22], a feature that can be further enhanced through the ability to genetically engineer their protein shell [23]. While the *in vitro* and *in vivo* US properties of GVs have been

characterized, it is crucial to understand their pharmacokinetic properties and excretion route as the basis from which to create targeted constructs and fully exploit their potential as molecular ultrasound contrast agents. Here, we report a mild and convenient methodology to functionalize and radiolabel GVs and the first quantitative spatio-temporal distribution study of radiolabeled GVs in mice using single photon emission computed tomography (SPECT) and quantitative tissue counting.

Material and Methods

Gas Vesicle Preparation

GV culturing, isolation and purification were carried out as previously described [17, 24]. In brief, *Halobacteria* sp. NCR-1 (Carolina Biological Supply, Burlington, NC) were cultured in high salt Carolina media, at 42 °C, in an incubation shaker at 100 revolution per minutes (rpm) (Ecotron, Infors AG, Switzerland). GVs were then isolated using TMC lysis buffer and purified through multiple rounds (5 to 6) of centrifugation at 300 rcf with the centrifuge maintained at 4 °C.

Radiolabeling of GVs with Technetium-99m

The technetium-99m-labeled tetrazine ([^{99m}Tc]Tz), compound 3 (Fig. 1a), was prepared following literature methods in good radiochemical yield and high purity (Suppl. Fig. S1a, b, in electronic supplementary material (ESM)) [25, 26]. Trans-cyclooctene (TCO)-conjugated GVs (TCO-GVs) were prepared by adding (E)-cyclooct-4-enyl-2,5-dioxopyrrolidin-1-yl carbonate (TCO-NHS) (855.1 μg, 3.2 μmol; Click Chemistry Tools, 1016-100) in dimethyl sulfoxide (DMSO, 197.3 μl) to a solution of GVs ($OD_{500\ nm}$ = 55.2, 1.8 ml) in PBS at pH 8. The solution was left to mix on a shaker for 2.5 h and the desired TCO-GVs purified by dialysis using 6–8 kD dialysis membrane submerged in PBS overnight (Spectra/Por 1 Dialysis Membrane, Spectrum Labs, USA). The TCO-GVs were then concentrated using centrifugal flotation at 300 rcf for 15 min (Fig. 1b). Compound 3 (29 MBq, 100 μl) was then added to a solution of TCO-GVs ($OD_{500\ nm}$ = 50, 400 μl) at room temperature and left shaking for 30 min. Tc-99m-labeled GVs ([^{99m}Tc]GVs) were then washed with PBS and purified from any residual 3 using a single round of centrifugal flotation (Fig. 1c). To assess the purity, a sample of the mixture was taken before and after purification, sonicated and injected into a HiTrap size-exclusion cartridge attached to a high-performance liquid chromatography (HPLC) fitted with a gamma detector. The column was eluted with 100 mM ammonium bicarbonate in water at 1 ml/min flow rate (isocratic elution 0–8 min 100 %).

Stability Study in Plasma

To determine the stability of [^{99m}Tc]GVs in plasma, samples were prepared following the procedures described above. To assess the purity, a sample of the mixture was taken and spotted on an iTLC-SG glass microfiber chromatography paper (Agilent Technologies, SGI0001) plate and run with a mobile phase of 75 % methanol, 25 % water, and visualized on a Bioscan AR-2000 Imaging Scanner. The purified [^{99m}Tc]GVs (3.4 MBq, 100 μl) was then added to mouse plasma (900 μl) and incubated on a shaker for 120 min at 37 °C. Samples were taken at 2, 5, 10, 20, 60, and 120 min and analyzed for purity by RadioTLC (Suppl. Fig. S2, ESM). At 60 and 120 min, 450 μl samples were taken, and the GV layer was

separated from the plasma by centrifugal flotation (400 rcf, 10 min). The activity in the plasma and GV layers was measured using a dose calibrator.

Biodistribution Studies

All experimental procedures were approved by the Animal Care Committees at Sunnybrook Research Institute and McMaster University.

Quantitative Tissue Counting

Studies were performed on healthy female, 5–6-week-old CD1 mice (Charles River Laboratory, Kingston, NY). Mice were injected intravenously (*i.v.*) with 0.7 MBq of [^{99m}Tc]Tz as a control or with 0.4 MBq of [^{99m}Tc]GVs *via* the tail vein. Mice were anesthetized with 3 % isoflurane and euthanized by cervical dislocation at 30, 60, 240, and 360 min for the control, while the [^{99m}Tc]GVs studies were performed at 5, 20, 60, and 120 min post-injection (n = 3 per time point). Blood, adipose, bone, brain, gall bladder, heart, kidneys, large intestine and cecum (with contents), liver, lungs, lymph nodes (axillary and brachial), pancreas, skeletal muscle, small intestine (with contents), spleen, stomach (with contents), thyroid/trachea, and bladder with urine and tail were collected, weighed, and counted in an automated gamma counter (PerkinElmer Wallac Wizard 1470 gamma counter, PerkinElmer, Waltham, USA). Decay correction was used to normalize organ activity measurements to time of dose preparation for data calculations with respect to the injected dose (reported as % injected dose (ID) per gram and % ID per organ).

SPECT/CT Imaging

Studies were performed following *i.v.* injection of intact or collapsed [^{99m}Tc]GVs at a constant flow rate of 500 μl/min (New Era Pump Systems, NE-1000, NY, USA) *via* the tail vein of healthy CD1 or SHO mice (Charles River Laboratory, 4–6 weeks of age, n = 6). Mice were anesthetized with isoflurane (2–2.5 % maintenance, Univentor 410, Univentor Ltd., Malta) and prepared for the GV injection. Collapsed GVs were obtained by reaching the collapse pressure inside a syringe (by capping the nozzle and pushing the piston). Once collapsed, GVs lose their ultrasonic contrast properties and cannot be investigated with ultrasound. Following catheterization, mice were placed in prone position on the mouse bed, which maintained its body temperature at 37 °C. The amount of activity injected ranged from 2.2 to 20.5 MBq. The volume injected ranged from 80 to 330 μl, and the concentration ranged from 18 to 33 $OD_{500\ nm}$. SPECT imaging was performed during and immediately after GV injection.

Fast dynamic whole body scans were performed on a SPECT imaging system (VECTor+, MILabs, Utrecht, The Netherlands) using a high-energy collimator (HE-UHR-RM, MILabs) with 156 clustered multi-pinholes collimator of 1.8 mm. An image was acquired prior to [^{99m}Tc]GVs injection. Following activity measurement in the syringe with a dose calibrator (Capintec Inc., NJ, USA), subsequent images were then collected by running the same acquisition with a scan time ranging from 33 to 84 s and for up to 120 min during and after injection of [^{99m}Tc]GVs. For calibration of SPECT images, a 1-ml syringe filled with a solution of known activity of [^{99m}Tc]GVs in PBS (measured by the dose calibrator for each experiment) was scanned using the same collimator after the animal experiment. To obtain

anatomical details, anesthetized mice were then scanned using an *in vivo* X-ray microtomography system (SkyScan 1176, Bruker Corp., Kontich, Belgium) at 35 μm pixel resolution and 360° scanning with a rotation step of 1.4° per image, 66 ms exposition time, 1 mm aluminum filter, 65 kV, and 385 μA.

SPECT/CT Data Processing and Statistical Analysis

All SPECT images were reconstructed using the pixel-based maximum likelihood expectation maximization (POSEM, VECTor+ software, MILabs, The Netherlands) algorithm using 16 subsets, 15 iterations, and a small voxel size of 0.512 mm^3 [27, 28]. During reconstruction, correction for scattering is performed using a triple-energy window method [29], *i.e.*, Tc-99m energy window with the photopeak window centered at the peak of the data set (142 keV), with a width set to 20 %, together with the left and right background windows centered at 125 and 159 keV, with a width set to 4.5 and 3.6 %, respectively. After reconstruction, the images were corrected for decay using the half-life of Tc-99m (6.02 h), attenuation correction was applied, and quantified SPECT images were obtained by using a calibration factor [30, 31]. Images were then processed using a semi-automatic segmentation based on the local mean analysis and 3D rendering tools in PMOD (PMOD Technologies LLC, v3.7, Zurich, Switzerland). Briefly, the segmentation method first separates the mouse body from the background noise using a histogram based algorithm. Secondly, the local mean time activity curve (TAC) and background noise are computed in the vicinities of selected points within mouse organs. Finally, the image is segmented into regions, which are merged according to their TACs in a hierarchical manner [32]. The resulting segmentation was checked slice by slice for imperfections, and any corrections including erosion, dilation, and/or deletion of voxels were made using PMOD morphological operations. TACs were generated according to individual segmented organs and are reported by averaging together data acquired within a time period of 10 min to yield the mean and associated standard error of the mean.

CT images were reconstructed using an implementation of the Feldkamp cone-beam algorithm and beam hardening, and ring artifacts were corrected in Nrecon (Bruker Corp.) [33]. The registration of CT and SPECT images and the movies were generated using PMOD Fusion tools (PMOD Technologies LLC).

Statistical analyses were performed using NCSS 11 (NCSS, LLC. Kaysville, UT, USA). All data are expressed as mean ± SEM where n is the number of observations in the dynamic *in vivo* SPECT biodistribution study. The reported standardized uptake values (%ID/cm^3) for each tissue were analyzed over the time period studied using two-sample test followed by a Mann-Whitney U test and a Kolmogorov- Smirnov test. An alpha error level of 5 % was used for the tests.

Fluorescence Imaging from Histology

GVs were labeled with a fluorophore (Alexa- 488, Sigma, USA) using standard amino-*N*-hydroxysuccinimide cross-linking [23]. Two healthy mice were injected *i.v.* either with Alexa-488 tagged GVs or native GVs (control) ($OD_{500\ nm}$ = 20, 130 μl) and euthanized 20 min following injection. The liver and spleen were collected, embedded in optimal cutting

temperature compound, and snap frozen in nitrogen, then stored in a − 80 °C freezer. Subsequently, the liver and spleen tissues were sectioned (4–5 μm, Cryostat, LEICA CM 3050 S, USA). Slides were then observed using an Olympus microscope (Olympus VS120 Virtual Slide Microscope, VS120-L100-W, ON, Canada) with identical acquisition parameters. Images were stored in the proprietary format and, later, visualized on a personal computer using OlyVIA (OLYMPUS OlyVIA 2.9). For each liver and spleen, up to three sections were observed.

Results

Radiolabeling

Most Tc-99m-labeling procedures require the use of reducing agents or harsh conditions [26, 34]; consequently, an indirect approach to radiolabel GVs was developed. The approach took advantage of the highly efficient and rapid bioorthogonal reaction between trans-cyclooctene and tetrazine [35]. First, excess of (E)-cyclooct-4-enyl-2,5-dioxopyrrolidin-1-yl carbonate (TCO-NHS) was added to GVs to react with the amine groups present on the GV shell. Any residual TCO-NHS was removed by dialysis and TCOGVs solution concentrated by centrifugal flotation. This was then followed by the addition of a novel [^{99m}Tc]Tz which was recently reported [25]. The [^{99m}Tc]Tz was first synthesized and isolated in a 45 % radiochemical yield and 99 % radiochemical purity. The [^{99m}Tc]Tz (140 MBq, 0.5 ml) was then added to a solution of TCO-GVs ($OD_{500\ nm}$ = 40, 1 ml) and incubated for 30 min at room temperature. The Tc-99m-labeled GVs ([^{99m}Tc]GVs) were then purified from any residual [^{99m}Tc]Tz *via* a simple centrifugation and washing step. With mild centrifugation (300 rcf, 5 min), the labeled GVs were easily isolated from residual [^{99m}Tc]Tz and formulated for injection. For quality control, a sample of the labeling mixture before and after purification was taken, sonicated, and injected into an HPLC system equipped with a size exclusion column and a gamma detector. The HPLC gamma trace of the crude mixture showed two broad peaks. The first one represents [^{99m}Tc]GVs (retention time = 2 min) while the second represents free [^{99m}Tc]Tz (3, retention time = 6 min) (Suppl. Fig. S1a, ESM). Following purification, the gamma trace only exhibited one peak representing [^{99m}Tc]GVs. The desired product was isolated in 59 % radiochemical yield with > 99 % radiochemical purity (Suppl. Fig. S1b, ESM).

The stability study revealed that, after incubation of the [^{99m}Tc]GVs in plasma at 37 °C for 120 min, there was little to no loss of the [^{99m}Tc]Tz from the surface of the GVs (Table S1, ESM). In addition, 31 % of GVs after 60 min are still intact, while the rest had either collapsed or had non-specific binding to plasma components (Table S2, ESM). The activity seen in the plasma layer is likely collapsed GVs rather than [^{99m}Tc]Tz based on the radioTLC data (Suppl. Fig. S2, ESM). This is consistent with the covalent nature of the bond between the components which is known to be stable *in vivo*.

Biodistribution: Ex Vivo Tissue Counting and SPECT

The distribution of [^{99m}Tc]GVs was evaluated by *ex vivo* tissue counting following necropsy and dynamic SPECT/CT imaging (video S1a and b, ESM). The tissue counting studies revealed, 5 min post [^{99m}Tc]GV injection, more than 5 % ID/g uptake in the gall bladder,

liver, lungs, spleen, and bladder/urine while all other mouse organs or fluids typically exhibited less than 2 % ID/g uptake (Fig. 2a). A small amount of [^{99m}Tc]GVs was detected in the blood 5 min following injection which eventually decreased to 0.5 % ID/ g after 2 h. Uptake at sites that showed early and high localization remained high throughout the duration of the study. The biodistribution of [^{99m}Tc]Tz alone also showed high gall bladder and small intestine concentrations, but there was significantly less activity in the liver, spleen, and lungs (particularly at later time points). It also showed faster blood clearance compared to [^{99m}Tc]GVs (Fig. 2b).

In Fig. 3, the 3D maximum intensity projections (MIP) of the *in vivo* dynamic SPECT data showed the spatial extent and signal intensity variations in the volume occupied by [^{99m}Tc]GVs in mouse organs at time points corresponding to those of the tissue counting studies. There was no large spatial variation in signal intensities observed 2 h following [^{99m}Tc]GVs injection; therefore, the spatial uptake of [^{99m}Tc]GVs in a given organ was relatively uniform. Overall, 3D MIP findings correlated with the *ex vivo* tissue counting biodistribution findings.

Likewise, *ex vivo* tissue counting and *in vivo* SPECT quantitative biodistributions were also in good overall agreement at the studied time points (Fig. 4), notably the reticuloendothelial system (RES) uptake (lungs, liver, spleen), the increase localization over time in the duodenum/small intestine, and the relatively short lived presence of GVs in the blood.

In Fig. 5a, 3D segmentation rendering of the mouse organs allowed the calculation of the volume occupied by [^{99m}Tc]GVs in each organ (Table S3, ESM). The volumes of these organs derived from the segmentation are similar to these found in healthy mice in the literature, *e.g.*, the liver and the gall bladder volumes [36, 37]. The *in vivo* dynamic uptake of [^{99m}Tc]GVs in segmented organs is reported in Fig. 5b. The overall uptake of native *versus* collapsed [^{99m}Tc]GVs by organs was similar. In addition, the change in the amount of activity and volume injected in mice did not alter the overall biodistribution of [^{99m}Tc]GVs in mouse organs and all SPECT data was therefore pooled together. Based on this data, [^{99m}Tc]GVs were rapidly taken up by the liver, spleen, and lungs, reaching a plateau within 10 min. In contrast, the uptake of [^{99m}Tc]GVs in the gall bladder peaked 20 min following injection and then significantly decreased for 30 min ($p = 0.001748$). The liver showed a peak value of 32 ± 3 % ID/ cm^3 at 8 ± 2 min (Fig. 5b). In contrast, [^{99m}Tc]GVs had a slow uptake in the duodenum for the first 20 min, but the uptake increased over time (Fig. 5b). [^{99m}Tc]GV uptake, reported as an average between 10 and 120 min in % ID/cm^3 ± SD, was consistently observed in the liver (30 ± 2), spleen (4 ± 1), lungs (11 ± 1), gall bladder (76 ± 24), as well as in the duodenum and small intestine (21 ± 7), and bladder (8 ± 4) (video S1a and b, ESM). The averaged uptake rate constant of the gall bladder was 2-, 4-, and 9-fold faster than the uptake rate constants of the liver, the lungs, and the spleen, respectively (Table S4, ESM).

Fluorescence Imaging

To confirm and better understand the spatial distribution of GVs at the microscopic level in liver and spleen tissues, fluorescence imaging on histology was performed. GVs were successfully tagged with Alexa-488 fluorophore (Alexa488-GVs) and were allowed to

circulate long enough to distribute in all mouse organs including in the small intestines. Native GVs did not exhibit any fluorescent signals in the liver or in spleen tissues. In contrast, there was a marked and consistent fluorescent signal from Alexa488-GVs in the liver and spleen tissues (Fig. 6).

Discussion

This study is the first to report the radiolabeling and biodistribution of GVs using both *ex vivo* tissue counting and SPECT imaging in mice. The labeling was performed using bioorthogonal chemistry between TCO-functionalized GVs and a Tc-99m-labeled tetrazine. The indirect approach avoided degradation of the GVs and non-specific labeling that could occur when using conditions typically employed during direct technetium labeling procedures. With this method, [^{99m}Tc]GVs were produced in a good radiochemical yield and high purity where the radiolabel-GV conjugate demonstrated high stability in plasma.

Twenty minutes following administration, the biodistribution and imaging studies of the labeled GVs in organs revealed that the reticuloendothelial system (RES) absorbed 84 % of native and collapsed [^{99m}Tc]GVs with the biliary system and small intestine assimilating the majority of the remaining material (13%). Almost no [^{99m}Tc]GVs remained in the blood 2 min after their injection, and they were more rapidly taken up by the gall bladder than the liver. Fluorescence imaging of the liver and spleen tissues further confirmed these findings.

RES Uptake

The uptake of radiolabeled GVs in non-target tissues is not surprisingly due to resident mature macrophages located close to the vesselwalls [38], removing [^{99m}Tc]GVs from blood circulation rapidly. Furthermore, uptake and retention in the liver, spleen, and lungs is likely from Kupffer, red pulp macrophages, and reticular cells, respectively, present in these tissues. Given the nanometer size, lemon shape, negatively charged surface (− 49 mV) of the *Halobacterium salinarum* GVs, and their low dispersibility/hydrophobicity [20], their rapid uptake by the RES was similar to other types of nanoparticles [39, 40]. Indeed, intact and degraded [^{99m}Tc]GV accumulation and saturation in the liver are likely due to their size since the liver sieve, *i.e.*, the existence of vascular fenestrations measuring 50–100 nm along the liver margin [41], would potentially facilitate non-specific uptake of individual radiolabeled GVs and degraded products. Likewise, [^{99m}Tc]GVs and degraded products were hardly taken up by the kidneys since only smaller-sized nanoparticles with diameters below 5 nm are filtered by the renal system when delivered intravenously [42]. Furthermore, the lemon shape and ability to change shape of the [^{99m}Tc]GVs, during gas exchange, could also be factors playing a role in biodistribution and, especially, in their spatial distribution in a given organ since Black *et al.* showed that differences in shape of radiolabeled gold nanoparticles clearly influenced their uptake and spatial distribution not only in tumors but also in the liver [43].

Gall Bladder and Intestine Uptake

Interestingly, uptake within the biliary system and intestines accounted for 13 % of [^{99m}Tc]GVs 20 min following administration. Of these organs, uptake in the gall bladder

and duodenum was seen immediately, with an increase in uptake in these organs up to 20 min post injection. Thereafter, uptake was observed in the rest of the small intestine. Since no [^{99m}Tc]GVs were observed in the stomach, these results suggest that radiolabeled GVs were captured by the hepatocytes in the liver, then secreted through the hepatic ducts and stored into the gall bladder. Assuming the endocytosis of [^{99m}Tc]GVs or [^{99m}Tc]GV fragments by hepatocytes, it is likely that radiolabeled GVs start degrading due to protease digestion in the liver. Likewise, the two times faster rate of uptake of [^{99m}Tc]GVs in the gall bladder would suggest some intact GVs reaching the gall bladder, followed by a similar degradation pathway of [^{99m}Tc]GV population to that in the liver. When the bile is secreted, further degraded radiolabeled GVs were likely subsequently released from the gall bladder to the duodenum through the common bile duct that joins the common hepatic duct and connects to the duodenum. Hence, the distribution in the gall bladder and small intestine is therefore likely explained by the size of individual radiolabeled GVs and/or cluster of radiolabeled GVs and of the presence of fragmented [^{99m}Tc]GVs that are all compounds too large to be cleared by the kidneys [42].

GVs as Potential Ultrasound Contrast Agent

The biodistribution studies showed a relatively short-lived presence of GVs in the blood. This limits the utility of native GVs for tumor imaging as GVs will likely not circulate long enough to extravasate into target tissues. Ongoing research efforts are focused on investigating the impact of shell alterations of native GVs on their biodistribution as well as the effect of pegylation of native and modified GVs on their pharmacokinetic properties. In addition, a better understanding of the integrity and degradation of radiolabeled GVs, in particular those with surface modifications to prolong circulation, will also need to be further investigated.

Notably, no acute toxicity or adverse effects in mice were observed in our study where up to five times higher concentrations were used than in previous studies [17]. However, more extensive toxicity studies on the optimal construct once developed will be needed prior to translation.

Conclusion

A convenient method for radiolabeling GVs with Tc-99m along with the first quantitative biodistribution study of [^{99m}Tc]GVs was reported. Results in healthy mice showed, not unexpectedly, a rapid uptake of radiolabeled GVs by the RES, providing a baseline for enhancing the *in vivo* properties of this novel class of ultrasound contrast agents. The reported labeling strategy conveniently offers the means to assess the impact of ongoing efforts associated with adding different pharmacokinetic modifiers and targeting molecules.

Supplementary Material

Refer to Web version on PubMed Central for supplementary material.

Acknowledgments

Funding Information JLF, MY, AF, MS, and SF acknowledge the financial support of the National Institutes of Health (NIH 1R01EB018975) and the Canadian Institutes for Health Research (CIHR MOP136842). AZ, HB, NJ, and JV acknowledge the financial support of Canadian Cancer Society (Innovation grant 2015:703857) and the Canadian Institutes for Health Research (CIHR/NSERC CHRP Grant 2016: 493840-16).

References

1. Abou-Elkacem L, Bachawal SV, Willmann JK. Ultrasound molecular imaging: moving toward clinical translation. Eur J Radiol. 2015; 84:1685–1693. [PubMed: 25851932]
2. Strobel D, Seitz K, Blank W, et al. Contrast-enhanced ultrasound for the characterization of focal liver lesions—diagnostic accuracy in clinical practice (DEGUM multicenter trial). Ultraschall Med. 2008; 29:499–505. [PubMed: 19241506]
3. Allendoerfer J, Tanislav C. Diagnostic and prognostic value of contrast-enhanced ultrasound in acute stroke. Ultraschall Med. 2008; 29:210–214.
4. Welschehold S, Geisel F, Beyer C, et al. Contrast-enhanced transcranial Doppler ultrasonography in the diagnosis of brain death. J Neurol Neurosurg Psychiatry. 2013; 84:939–940. [PubMed: 23584493]
5. Siracusano S, Bertolotto M, Ciciliato S, et al. The current role of contrast-enhanced ultrasound (CEUS) imaging in the evaluation of renal pathology. World J Urol. 2011; 29:633–638. [PubMed: 21604017]
6. Wilson SR, Burns PN. Microbubble-enhanced US in body imaging: what role? Radiology. 2010; 257:24–39. [PubMed: 20851938]
7. D'Onofrio M, Canestrini S, De Robertis R, et al. CEUS of the pancreas: still research or the standard of care. Eur J Radiol. 2015; 84:1644–1649. [PubMed: 25796427]
8. Lindner JR. Molecular imaging of cardiovascular disease with contrast-enhanced ultrasonography. Nat Rev Cardiol. 2009; 6:475–481. [PubMed: 19506587]
9. Mulvagh SL, Rakowski H, Vannan MA, et al. American Society of Echocardiography consensus statement on the clinical applications of ultrasonic contrast agents in echocardiography. J Am Soc Echocardiogr. 2008; 21:1179–1201. quiz 1281. [PubMed: 18992671]
10. Smeenge M, Tranquart F, Mannaerts CK, et al. First-in-human ultrasound molecular imaging with a VEGFR2-specific ultrasound molecular contrast agent (BR55) in prostate cancer. Investig Radiol. 2017; 52:419–427. [PubMed: 28257340]
11. Tranquart F, Arditi M, Bettinger T, et al. Ultrasound contrast agents for ultrasound molecular imaging. Z Gastroenterol. 2014; 52:1268–1276. [PubMed: 25390214]
12. Willmann JK, Bonomo L, Carla Testa A, et al. Ultrasound molecular imaging with BR55 in patients with breast and ovarian lesions: first-in-human results. J Clin Oncol. 2017; 19:2133–2140. DOI: 10.1200/JCO.2016.70.8594
13. Liu J, Levine AL, Mattoon JS, et al. Nanoparticles as image enhancing agents for ultrasonography. Phys Med Biol. 2006; 51:2179–2189. [PubMed: 16625034]
14. Lanza GM, Wallace KD, Scott MJ, et al. A novel site-targeted ultrasonic contrast agent with broad biomedical application. Circulation. 1996; 94:3334–3340. [PubMed: 8989148]
15. Kripfgans OD, Fowlkes JB, Miller DL, et al. Acoustic droplet vaporization for therapeutic and diagnostic applications. Ultrasound Med Biol. 2000; 26:1177–1189. [PubMed: 11053753]
16. Martinez HP, Kono Y, Blair SL, et al. Hard shell gas-filled contrast enhancement particles for colour Doppler ultrasound imaging of tumors. Med Chem Commun. 2010; 1:266–270.
17. Shapiro MG, Goodwill PW, Neogy A, et al. Biogenic gas nanostructures as ultrasonic molecular reporters. Nat Nanotechnol. 2014; 9:311–316. [PubMed: 24633522]
18. Walsby AE, Hayes PK. Gas vesicle proteins. Biochem J. 1989; 264:313–322. [PubMed: 2513809]
19. Pfeifer F. Distribution, formation and regulation of gas vesicles. Nat Rev Microbiol. 2012; 10:705–715. [PubMed: 22941504]
20. Walsby AE. Gas Vesicles. Microbiol Rev. 1994; 58:94–144. [PubMed: 8177173]

21. Cherin E, Melis JM, Bourdeau RW, et al. Acoustic behavior of Halobacterium salinarum gas vesicles in the high-frequency range: experiments and modeling. Ultrasound Med Biol. 2017; 43:1016–1030. [PubMed: 28258771]
22. Maeda H, Nakamura H, Fang J. The EPR effect for macromolecular drug delivery to solid tumors: improvement of tumor uptake, lowering of systemic toxicity, and distinct tumor imaging in vivo. Adv Drug Deliv Rev. 2013; 65:71–79. [PubMed: 23088862]
23. Lakshmanan A, Farhadi A, Nety SP, et al. Molecular engineering of acoustic protein nanostructures. ACS Nano. 2016; 10:7314–7322. [PubMed: 27351374]
24. Lakshmanan A, Lu GJ, Farhadi A, et al. Preparation of biogenic gas vesicle nanostructures for use as contrast agents for ultrasound and MRI. Nature Protocols. 2017; 12:2050–2080. DOI: 10.1038/nprot.2017.081 [PubMed: 28880278]
25. Bilton HA, Ahmad Z, Janzen N. , et al. Preparation and evaluation of 99mTc-labeled tridentate chelates for pre-targeting using bioorthogonal chemistry. J Vis Exp. 2017.
26. Maresca KP, Marquis JC, Hillier SM, et al. Novel polar single amino acid chelates for technetium-99m tricarbonyl-based radiopharmaceuticals with enhanced renal clearance: application to octreotide. Bioconjug Chem. 2010; 21:1032–1042. [PubMed: 20402463]
27. van der Have F, Vastenhouw B, Rentmeester M, Beekman FJ. System calibration and statistical image reconstruction for ultra-high resolution stationary pinhole SPECT. IEEE Trans Med Imaging. 2008; 27:960–971. [PubMed: 18599401]
28. Branderhorst W, Vastenhouw B, Beekman FJ. Pixel-based subsets for rapid multi-pinhole SPECT reconstruction. Phys Med Biol. 2010; 55:2023–2034. [PubMed: 20299722]
29. Ogawa K, Harata Y, Ichihara T, et al. A practical method for position-dependent Compton-scatter correction in single photon emission CT. IEEE Trans Med Imaging. 1991; 10:408–412. [PubMed: 18222843]
30. Wu C, Van Der Have F, Vastenhouw B, et al. Absolute quantitative total-body small-animal SPECT with focusing pinholes. Eur J Nucl Med Mol Imaging. 2010; 37:2127–2135. [PubMed: 20577738]
31. Wu C, de Jong JR, Gratama van Andel HA, et al. Quantitative multi-pinhole small-animal SPECT: uniform versus non-uniform Chang attenuation correction. Phys Med Biol. 2011; 56:N183–N193. [PubMed: 21865622]
32. Maroy R, Boisgard R, Comtat C, et al. Segmentation of rodent whole-body dynamic PET images: an unsupervised method based on voxel dynamics. IEEE Trans Med Imaging. 2008; 27:342–354. [PubMed: 18334430]
33. Feldkamp LA, Davis L, Kress J. Practical cone-beam algorithm. J Opt Soc Am A. 1984; 1:612–619.
34. James S, Maresca KP, Allis DG, et al. Extension of the single amino acid chelate concept (SAAC) to bifunctional biotin analogues for complexation of the M(CO) 3 +1 Core (M = Tc and Re): syntheses, characterization, biotinidase stability, and avidin binding. Bioconjug Chem. 2006; 17:579–589. [PubMed: 16704194]
35. Blackman ML, Royzen M, Fox JM. Tetrazine ligation: fast bioconjugation based on inverse-electron-demand Diels-Alder reactivity. J Am Chem Soc. 2008; 130:13518–13519. [PubMed: 18798613]
36. Al-Azzawi HH, Mathur A, Lu D, et al. Pioglitazone increases gallbladder volume in insulin-resistant obese mice. J Surg Res. 2006; 136:192–197. [PubMed: 17045610]
37. Melloul E, Raptis DA, Boss A, et al. Small animal magnetic resonance imaging: an efficient tool to assess liver volume and intrahepatic vascular anatomy. J Surg Res. 2014; 187:458–465. [PubMed: 24342872]
38. Kaminskas LM, Boyd BJ. Nanosized drug delivery vectors and the reticuloendothelial system. In: Prokop A, editorIntracellular Delivery. Fundamental Biomedical Technologies. Vol. 5. Springer; Dordrecht: 2011.
39. McNeil SE. Nanoparticle therapeutics: a personal perspective. Wiley Interdiscip Rev Nanomed Nanobiotechnol. 2009; 1:264–271. [PubMed: 20049796]
40. Nel AE, Mädler L, Velegol D, et al. Understanding biophysicochemical interactions at the nano-bio interface. Nat Mater. 2009; 8:543–557. [PubMed: 19525947]

41. Braet F, Wisse E, Bomans P, et al. Contribution of high-resolution correlative imaging techniques in the study of the liver sieve in three-dimensions. Microsc Res Tech. 2007; 70:230–242. [PubMed: 17279510]

42. Choi HS, Liu W, Misra P, et al. Renal clearance of quantum dots. Nat Biotechnol. 2007; 25:1165–1170. [PubMed: 17891134]

43. Black KCL, Wang Y, Luehmann HP, et al. Radioactive 198Audoped nanostructures with different shapes for in vivo analyses of their biodistribution, tumor uptake, and intratumoral distribution. ACS Nano. 2014; 8:4385–4394. [PubMed: 24766522]

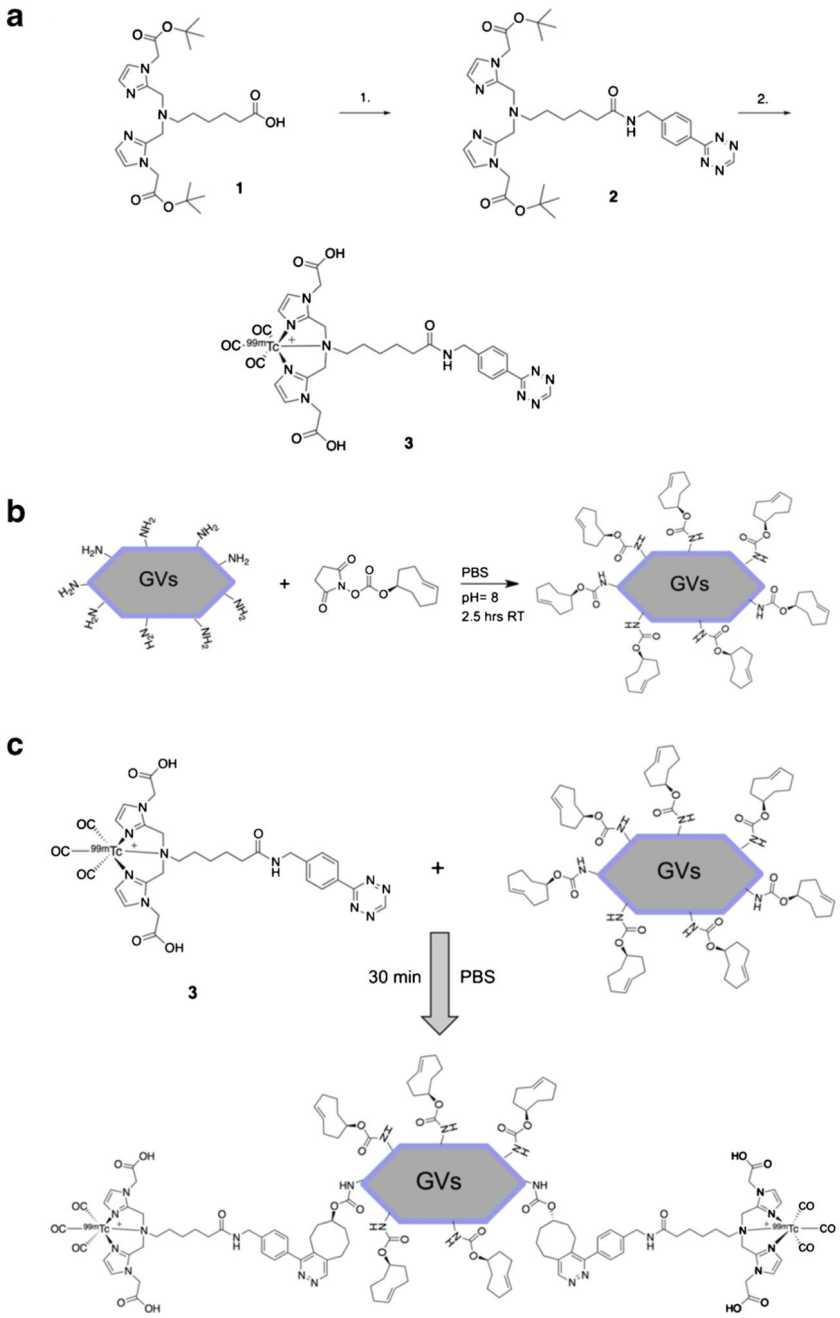

Fig. 1.

Radiolabeling methodology and processes. **a** Synthesis of [^{99m}Tc]tetrazine complex 3. (1) PyBOP, DIPEA, DMF, ((4-tetrazine-3-yl)phenyl)methanamine hydrochloride, rt., 12 h (2) (i) [[^{99m}Tc](CO)$_3$(H$_2$O)$_3$]+, MeOH, saline, 60 °C (MW), 20 min. (ii) TFA, DCM, 60 °C (MW), 6 min. **b** Representation of the chemistry used to prepare TCO-conjugated GVs. TCO-GVs were purified by dialysis and concentrated to an optical density ($OD_{500\ nm}$) of 40. **c** Chemistry used to label TCO-GVs with compound 3. Tc-^{99m}-labeled Tz (3) was added to TCO-GVs in PBS for 30 min and the [^{99m}Tc]GVs purified by centrifugal flotation.

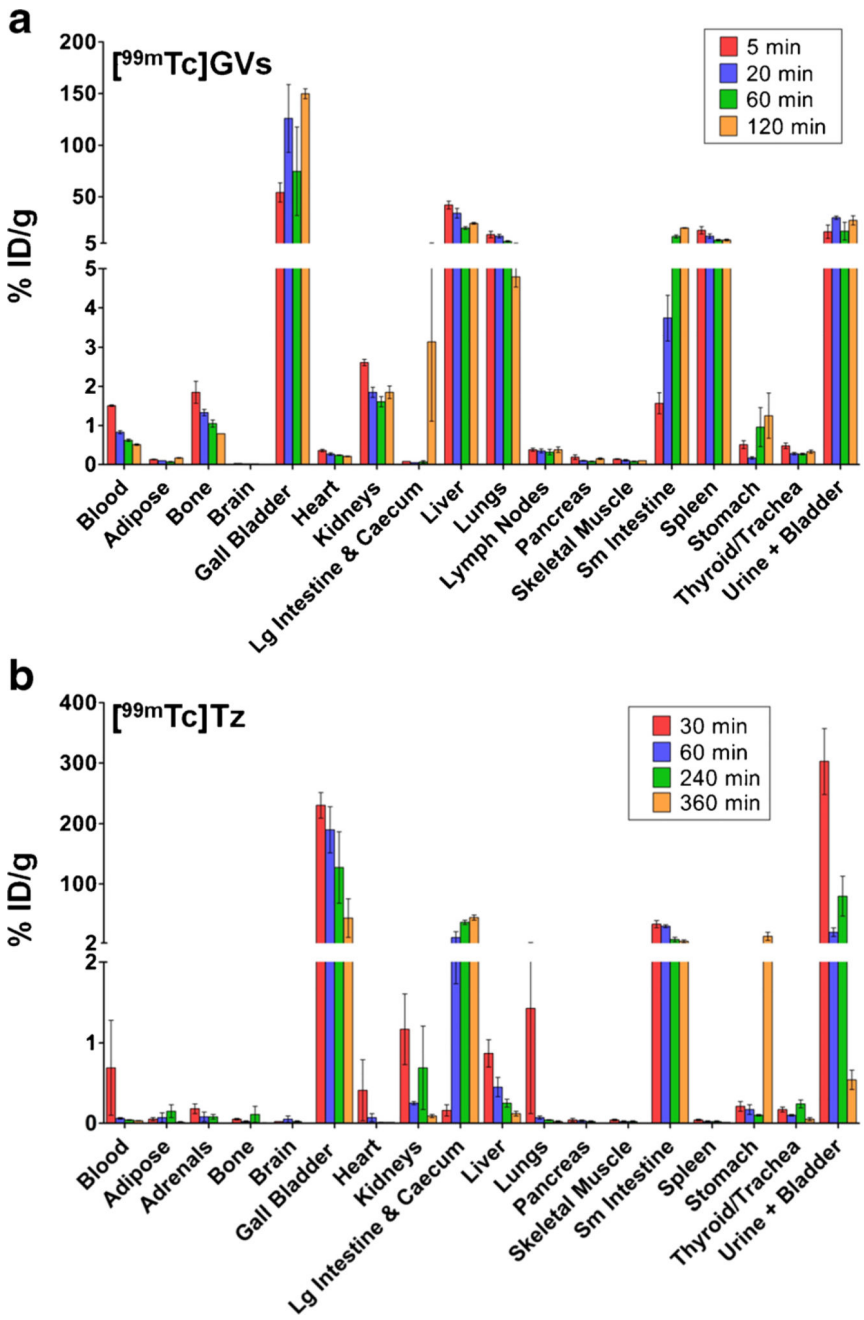

Fig. 2.

Quantitative *ex vivo* tissue counting biodistribution data for [^{99m}Tc]GVs and [^{99m}Tc]Tz (3). Groups of mice (n = 3/time point) were euthanized at 5, 20, 60, and 120 min([^{99m}Tc]GVs) or at 30, 60, 240, and 360 min ([^{99m}Tc]Tz). Tissues and fluids were then collected and activity counted. **a** The uptake of [^{99m}Tc]GVs was mainly found in the gall bladder, liver, lungs, small intestine, spleen, and bladder. **b** In contrast, [^{99m}Tc]Tz was mainly found in the gall bladder, small intestine, large intestine and cecum, and bladder. Data are reported in % injected dose (ID)/g ± SEM.

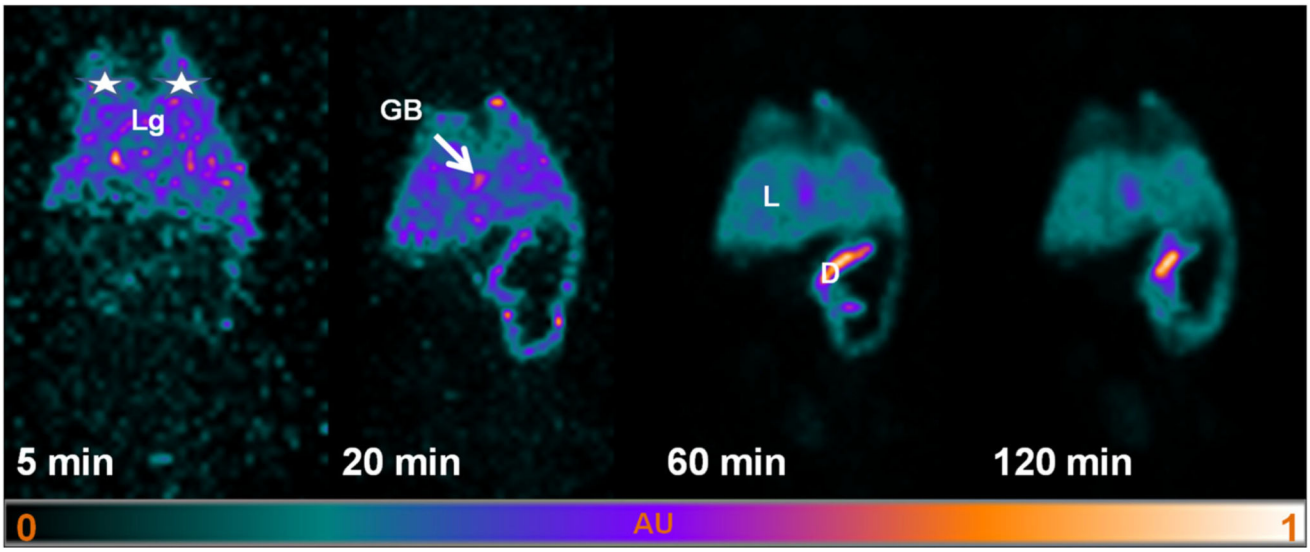

Fig. 3.

Maximum intensity projection (MIP) of SPECT images following [^{99m}Tc]GVs injection. Rapid uptake of [^{99m}Tc]GVs is shown in the lungs (white stars, Lg), gall bladder (GB) and liver (L), followed by duodenum (D) and small intestines over time.

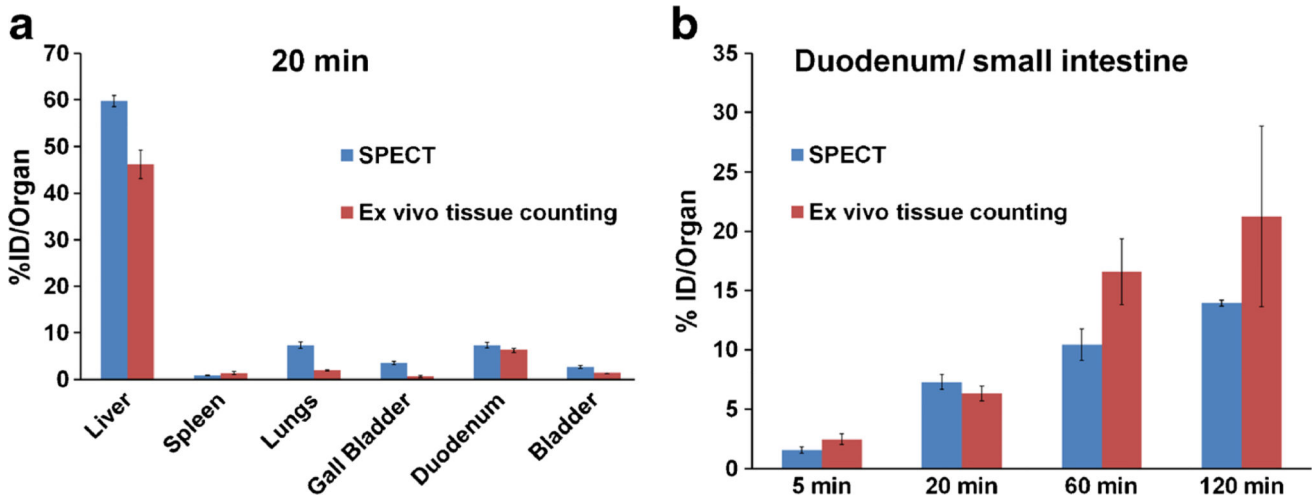

Fig. 4.

Ex vivo tissue counting and SPECT biodistribution. **a** Comparison of both biodistribution data reporting the uptake of [^{99m}Tc]GVs in major organ/tissues 20 min following injection. **b** [^{99m}Tc]GVs uptake in the duodenum (SPECT) and small intestine (*ex vivo* tissue counting) showing a similar increase at corresponding time points (4 time points, $n = 3$ per time point). Each SPECT reported values were calculated using the segmentation results multiplied by the volume of the corresponding segmented organ. Data are reported in %ID/organ ± SEM (*Ex vivo* counting data is not normalized for weight, 4 time points, $n = 3$ per time point, SPECT $n = 23$, 55, 31, and 8 at 5, 20, 60, and 120 min, respectively.).

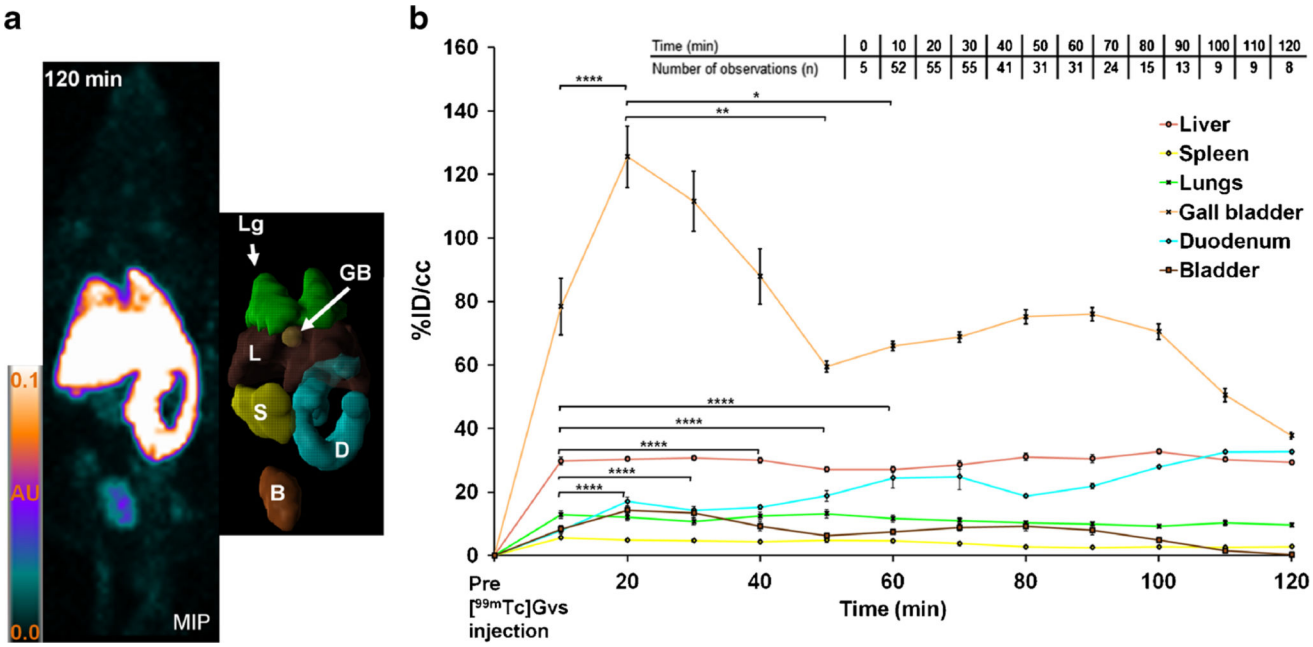

Fig. 5.

MIP, 3D segmentation, and time activity curves (TACs) of segmented organs. **a** MIP of SPECT data and associated 3D segmentation of individual organs at 120 min (lungs in green (Lg), liver in brown (L), gall bladder (GB) in light orange, spleen (S) in yellow, duodenum in light blue (D), and bladder in light brown (B)). **b** TACs showed the uptake of [^{99m}Tc]GVs in segmented organs. TACs are reported in percent injected dose per volume of tissue (%ID/cm^3) by averaging together data acquired within a time periods of 10 min to yield the mean and associated standard error of the mean (SEM). The inset shows the number of observations (n) for each time point. Significant statistical differences are only shown for the gall bladder and duodenum for each data point between 10 and 60 min (*$p \leq 0.05$, **$p \leq 0.01$, ****$p \leq 0.0001$).

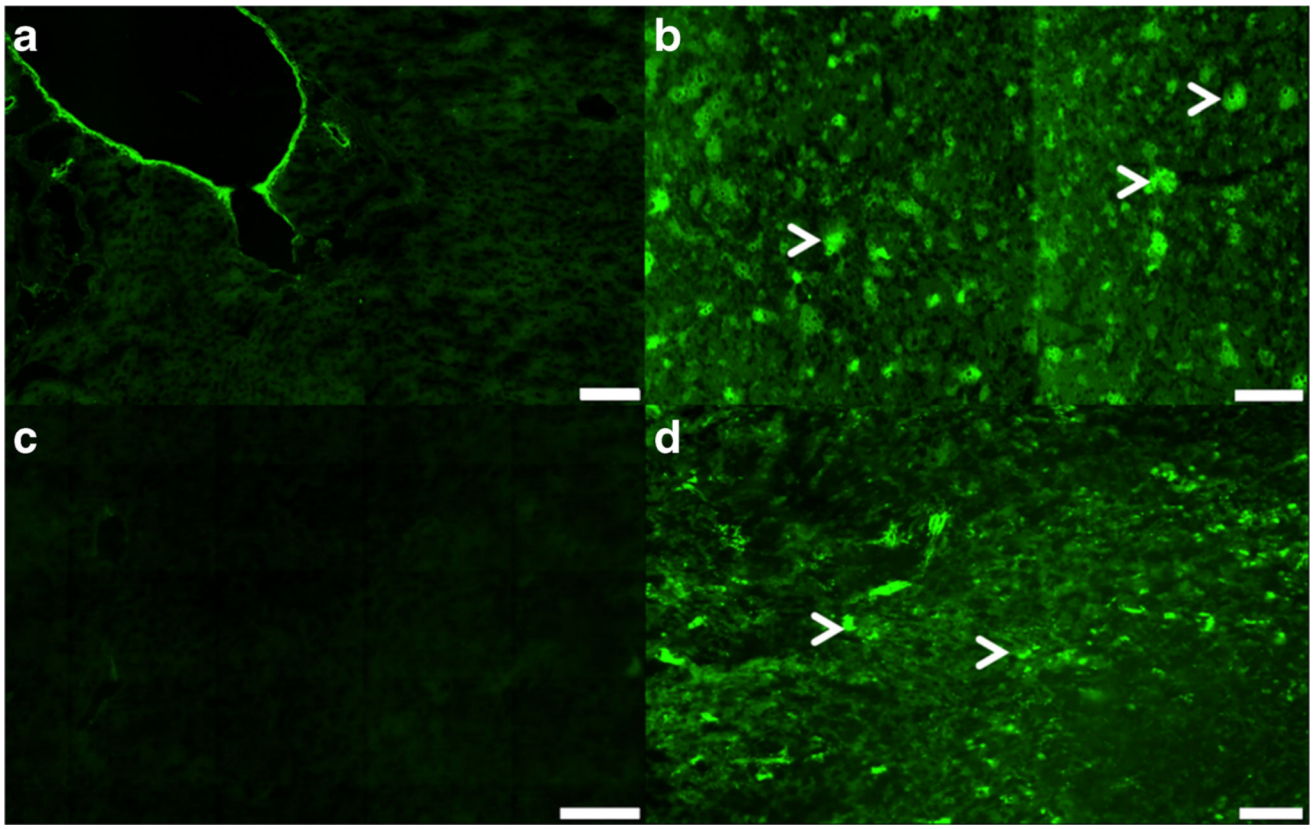

Fig. 6.

Fluorescence imaging of the liver and spleen tissues. Native GVs in **a** the liver and in **c** the spleen tissues showing only autofluorescence. Alexa 488 fluorophore tagged GVs in **b** the liver and **d** spleen tissues showing an increase green signal intensity. White arrows show clustering of Alexa488-GVs in both tissues. Scale bar is 100 μm (**a–c**) and 50 μm (**d**). Magnification: × 20 (**a, c**) and × 10 (**b, d**).